Micro-Nano Hierarchical Micropattern-Enhanced Antifogging Surface Inspired by Tree Frogs

AUTHOR INFORMATION

Mingsheng Li[†], Haibao Hu*[†], Liuzhen Ren[†], Mengzhuo Zhang[†], Jun Wen[†], Laibing Jia[‡], Xiaopeng Chen[†]

† School of Marine Science and Technology, Northwestern Polytechnical University, Xi’an 710072, China

‡ Department of Naval Architecture, Ocean and Marine Engineering, University of Strathclyde, Glasgow G4 0LZ, UK

*Corresponding author: E-mail: huhaibao@nwpu.edu.cn (H. Hu).

ABSTRACT

Fogging on glass is common but can also be dangerous when it occurs on eyeglasses, camera lenses, mirrors, and windshields of automobiles and airplanes. Inspired by the toe pads of tree frogs in nature, biomimetic structures in the form of regular arrays of micro-hexagonal prisms were fabricated. Common UV lithography, ion-beam etching, and neutral loop discharge were used to construct these arrayed microstructures. Chemical etching was then used to create various scale nanostructures to provide better wettability in the microchannel between the micro-hexagonal prisms and optical properties on the top surface of the micro-hexagonal prisms. The wettability, optical characteristics, and antifogging performance of the biomimetic antifogging gradient (BAFG) surface were tested experimentally. The BAFG surface exhibited excellent antifogging and optical properties; this stimulated the preferential formation of a water film network in the microchannel and facilitated the spreading of a stable water film on the surface. Remarkably, the transmittance of the BAFG surface reached 99% of the transmittance of the bare glass. The average transmittance for the bare glass (68.7%) under fog conditions improved to approximately 94.4% for the BAFG surface. Three stages for the condensation of vapor and the formation of the water film were described according to thermodynamic theories, which elucidate the internal mechanism.

KEYWORDS: biomimetic surface; antifogging; wetting gradient; micro-hexagonal prism array.

DECLARATION OF COMPETING INTEREST

The authors declare no competing financial interest.

This is a peer-reviewed, accepted author manuscript of the following paper: Li, M., Hu, H., Ren, L., Zhang, M., Wen, J., Jia, L., & Chen, X. (Accepted/In press). Micro-nano hierarchical micropattern-enhanced antifogging surface inspired by tree frogs. Applied Physics A: Materials Science and Processing.

1. INTRODUCTION

Fogging on glass is a common phenomenon in daily life. However, it can disrupt the normal operation of eyeglasses, goggles, camera lenses and mirrors. Fogging poses a severe danger to the safe operation of airplanes and automobiles due to windshield visibility [1-7]. Earlier studies have reported that, when the temperature of a solid surface is less than or equal to the dew point temperature, the water vapor in the air transforms into small and discrete liquid droplets on the solid surface [8]; this scatters the incident light in all directions and results in visual blurring by changing the structure of the glass surface [9]. Superhydrophilic surfaces, with apparent contact angles of less than 5° [10], have been investigated to address this problem owing to their unique wetting properties; such surfaces allow the water vapor in the air to condense on them in the form of a thin water film rather than discrete droplets. The thin water film reduces the scattering of incident light.

Hierarchical microstructure materials have been widely investigated and applied in microfluidics [11, 10, 12-19] and energy conversion and storage fields [20-32] over the years owing to their high specific surface area. Wenzel reported that the surface roughness could significantly enhance the wettability because the solid–liquid interface area on a rough surface is larger than the apparent contact area [11, 12]. Various methods have been used to fabricate rough surfaces, such as chemical etching [10, 13, 14], dry etching [15], laser structuring [16, 17], vapor deposition [18, 19], and charge injection [33]. Xiong et al. [10] demonstrated a simple method for creating nanostructures on glass through an alkali corrosion process to enhance transparency and achieve antifogging characteristics. Additionally, they investigated the morphology of glasses with different compositions and alkali etching times. Du and He [13] described a simple method for manufacturing a uniform porous structure coupled with nanoflakes on a glass surface using a sodium hydroxide solution etching process; they further discussed the relationship between alkali concentration and nanoflake thickness. Fujima et al. [14] used a heated sodium bicarbonate solution as the etching medium and developed a hierarchical nanoporous layer on silicate glass, through which they realized antifogging and antifouling functionalities.

Biomimetic hierarchical structures with enhanced wettability properties have also been widely investigated over the last two decades. For example, the lotus leaf [34, 35] and water strider legs [36], which exhibit excellent water repellency and self-cleaning properties, as well as the compound eyes of insects [37, 38] and butterfly wings [39], have been investigated for their antifogging performance arising from their hierarchical structures. In particular, Feng et al. [40] and Dudukovic et al. [41] conducted novel research that established a new direction for "cellular fluidics" and further eliminated water accumulation for antifogging. However, creating a balance between the surface wettability and optical properties and achieving an excellent diffusivity of water for longstanding antifogging properties are highly challenging.

The toe pads of tree frogs have been studied for their superior wet attachment and friction performance in the absence of an external force. Studies have shown that these superior properties arise from the enhanced water diffusivity induced by the micro-hexagonal prisms on the top surface of the toe pads; this causes an increase in the wettability of the toe pad surface [42-46]. Inspired by the toe pads of tree frogs, a mimicking structure in the form of a regularly arranged micro-hexagonal prism array was developed and the balance between the properties of wettability and transmittance was optimized to some extent. The array was etched with a potassium hydroxide (KOH) solution for different times in the microchannels between micro-hexagonal prisms and the top surface of the micro-hexagonal prisms to create a wettability gradient; this showed high transmittance from the top surface of the micro-hexagonal prisms and better wettability properties in the microchannels between micro-hexagonal prisms. The water condensed on the surface was efficiently drained by the arrayed microstructure due to its excellent diffusivity; this improved the antifogging property. Furthermore, the water condensed in the microchannels between the micro-hexagonal prisms created a network of water films that connected the tiny plates together. Naturally, the tiny plates reduced the embryo growth time to connect the water network; this caused the formation of a stable water film on the biomimetic anti-fog gradient (BAFG) surface in a short time.

The wettability and transmittance properties were optimized by adjusting the projected surface area fraction of the microchannels between the micro-hexagonal prisms. Additionally, the wettability, optical characteristics and antifogging properties of the BAFG surface were investigated in detail. The optical performance was quantitatively tested by exposing the BAFG surface to steam; this significantly improved the optical transparency and surpassed that of the BAFG surface itself. To investigate the antifogging mechanism, the entire condensation process of the BAFG surface was recorded; this showed that the BAFG surface was more conducive to the formation of a water film than the bare glass.

2. MATERIAL AND METHODS

2.1 Materials

Glass slides (bf33) were purchased from SCHOTT Co. Analytical reagent-grade ethanol, acetone, positive photoresist and KOH were purchased from commercial sources and were used without further purification. The elastomer, polydimethylsiloxane (PDMS) sylgard 184, was purchased from Dow Corning. Deionized water was used in all experiments.

2.2 Fabrication of BAFG surface

The biomimetic surface structure was fabricated by dry etching using the following procedure. Initially, the glass was cleaned with ethanol and acetone under ultrasonication for 30 min and washed with deionized water (Fig. 1). Next, a Cr film of thickness 300 nm was sputtered on a glass substrate via physical vapor deposition (ULVAC ei-5, rates: 1.68 A/s, power: 50 kW, vacuum degree: 5×10^{-4} Pa, temperature: 70 °C). Subsequently, a 2-μm positive photoresist (az5214) film was spun onto the Cr film; this was followed by a common lithographic process to fabricate the pattern and mark the locations of the microstructures on the Cr film. Ion beam etching was applied to etch the bare surface of Cr uncovered by the photoresist using a base pressure of 5.0×10^{-4} Pa, an operating vacuum of 2×10^{-2} Pa to a final vacuum of 4.3×10^{-5} Pa at a test temperature of 20 °C and an ion energy of 350 eV. A portion of the glass substrate that was not protected by Cr and the photoresist film was etched using a neutral loop discharge. To prevent KOH corrosion, the backside of the glass substrate was covered by PDMS; the weight ratio of the pre-polymer and curing agent was 10:1. A 15 g mixture was poured over the backside of the substrate and heated at 80 °C for 3 h. The glass substrate was then placed in a 0.5 M KOH solution; this was heated to 95 °C for 12 h to fabricate the nanostructure [10] and remove the photoresist. After etching and removing the photoresist, the prepared substrate was submerged in a Cr corrosive liquid to remove the Cr film. Finally, the glass substrate with the pattern was submerged in a 0.1 M KOH solution at 95 °C for 1 to 3 h. After removing the PDMS, cleaning with deionized water, and drying with a gas stream, the gradient surface, which was textured with a biomimetic microstructure and random nanostructure, was completed; to verify the reproducibility of the method, each step was repeated three times and the substrate was observed and tested. To compare the transmittance and antifogging properties of the different biomimetic surfaces, micro-hexagonal pillar patterns were designed with four circumcircle diameters (50, 100, 150 and 200 μm), four microchannel widths (2, 4, 6 and 8 μm), and a microchannel depth of 1 μm, which was chosen based on workability and optical properties [13]. The different substrates are called X-Y, using X for the different circumcircle diameters and Y for the different microchannel widths with "-" as the joint mark.

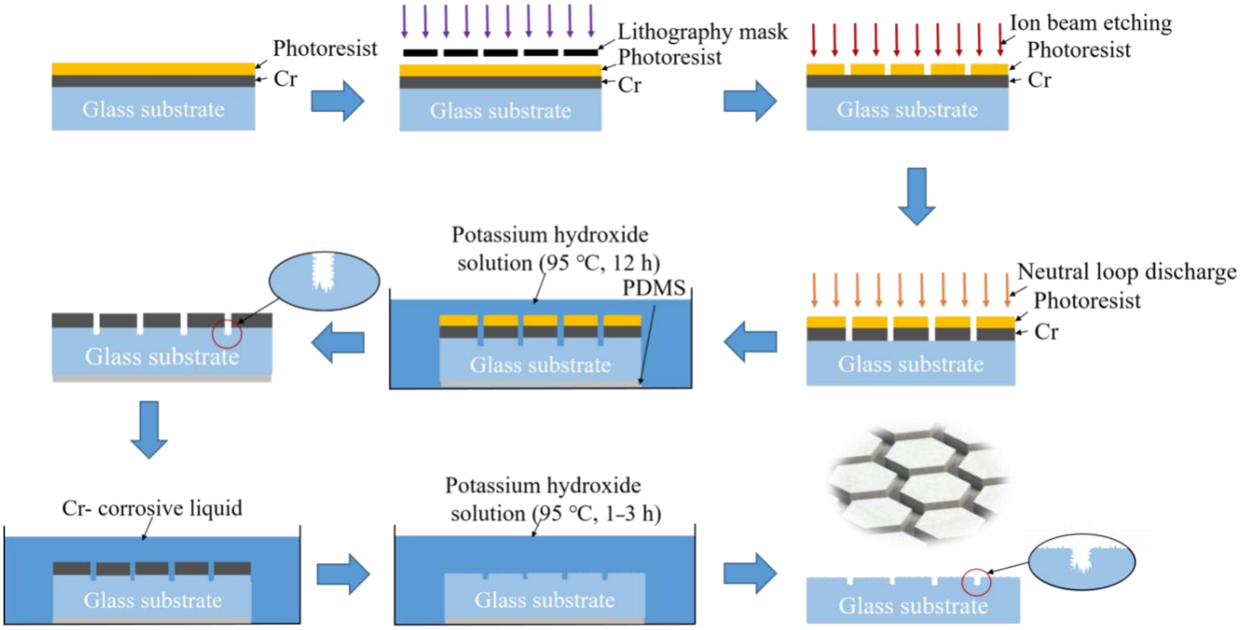

Fig. 1 Structure fabricated by masked dry etching and alkali corrosion

2.3 Characterization

The morphology of the biomimetic surface was determined by scanning electron microscopy (SEM, FEI Quanta FEG 250). The water contact angle of the BAFG surface was measured using an optical contact angle device (OCA 15EC, Dataphysics, Germany) with a test droplet volume of 4 μL. To study the optical properties, the transmittance of the surface was recorded using a spectrophotometer (4802 UV/VIS) in the wavelength range of 390 and 780 nm. The condensation process was recorded using a digital microscope (Model B011, Shenzhen Supereyes Technology Co. Ltd, China) in an ambient environment at a room temperature of 25 °C and a relative humidity of 55%.

3. RESULTS AND DISCUSSION

3.1 Morphology

The structure of the BAFG surface was observed using SEM. Fig. 2 shows the micro-hexagonal prisms on the tree frog toe pads and SEM images of the artificial biomimetic microstructure. Figs. 2a and b [46] show enlarged SEM images of the toe pads, which are clearly covered with micro-hexagonal structures. The diameter of the outer circle of the micro-hexagon was approximately 10 μm and the width of the microchannel between the micro-hexagonal prisms was approximately 1 μm. Utilizing this unique structure, we designed and fabricated a biomimetic structure using the 3D model images shown in Figs. 2c and S1. The height of the micro-hexagonal prism was 1 μm. The diameters of the outer circles of the micro-hexagons were 50, 100, 150 and 200 μm, while the widths of the microchannels were 2, 4, 6 and 8 μm. A top view of the BAFG surface is shown in

Fig. 2d. The as-fabricated substrate was immersed in a KOH solution (0.5 M) for 12 h and heated to 95 ℃ to produce the nanostructure, as shown in Fig. 2e. After etching with a KOH solution for 12 h, the surface of the glass was filled with granular particles (10–100 nm). Fig. 2f shows the nanostructure on the top surface of the micro-hexagonal prisms, which were etched by a 0.1 M KOH solution for 3 h. The nanostructure on the top surface of the micro-hexagonal prisms was much smaller than that in the microchannel; this created a wettability gradient. The influence of the corrosion time on the nanostructure and wettability was also investigated. Fig. S3 shows that as the corrosion time increased, the nanostructure became larger, and the water contact angle decreased.

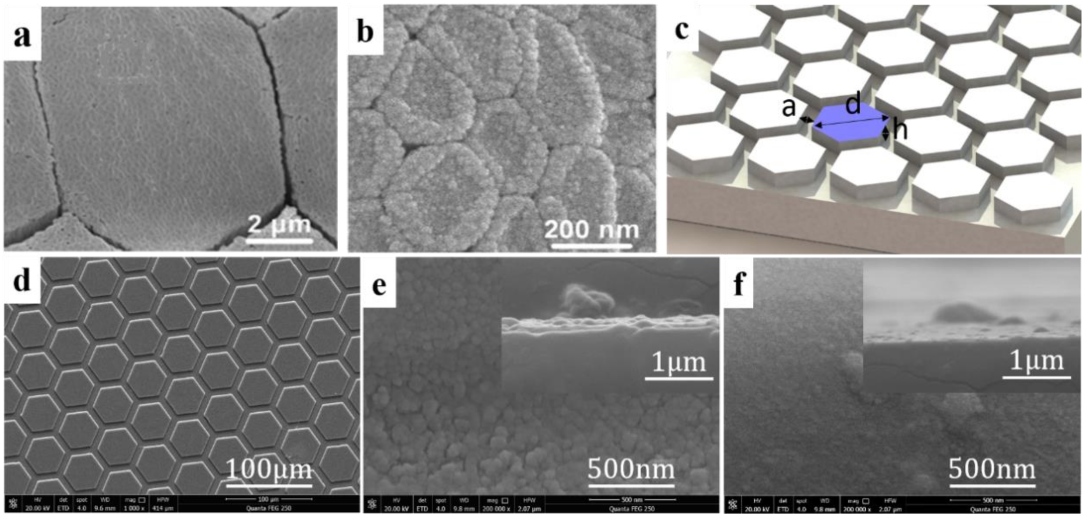

Fig. 2 a, b SEM images [46] of the toe pads of the tree frog. **c** 3D illustration of the BAFG surface layout. The surface marked in blue is the top surface of a micro-hexagonal prism. The microchannels exist between neighboring prisms. **d** Low-magnification SEM image of the BAFG surface. **e** Enlarged SEM image of the nanostructure in the microchannel (top and side views). **f** Enlarged SEM image of the nanostructure in the top surface of the micro-hexagonal prisms (top and side views)

3.2 Wettability of the biomimetic surface

Wenzel [11] noted that the roughness of a surface significantly enhanced its hydrophilicity. The apparent contact angle (CA) can be calculated using the Wenzel equation for a rough surface as shown below:

$$\cos\theta_w = \phi\cos\theta, \tag{1}$$

where θ_w denotes the apparent CA on the structured surface, θ denotes the intrinsic CA on the smooth surface and ϕ denotes the roughness parameter defined as the ratio of the practical surface and projected areas. The parameter, $\phi,$ is high for an etched surface; hence, the droplet can reach a state of complete wetting. The wettability of the biomimetic surface was investigated by measuring the CA; the test droplet volume was 4 μL. We measured the biomimetic surface with a circumcircle diameter of 50 μm and microchannel widths of 2, 4, 6 and 8 μm, etched by the KOH solution (Fig. 3); the substrates were tested at least three times and the results were averaged to account for errors. When the droplet was added onto the prepared surface, the apparent CA was approximately 70°; as the etching time increased, the CA decreased. Furthermore, there were no significant differences in the CA for different microchannel widths. This was because the differences in the microchannel widths were much smaller than the diameter of the test droplet; the microstructure etched by KOH at the edge of the hexagonal prism had different effect on the three contact lines of the droplet, leading to a random change in the droplet contact angle. However, an appreciable enhancement in hydrophilicity was obtained with all microchannel widths in comparison with the hydrophilicity of the slide glass etched for 3 h (Fig. S1). This was because the nanostructure was induced by chemical corrosion and the hydroxyl groups introduced by the alkali solution; this led to a high surface energy. In addition, we tested the surface chemical compositions using X-ray photoelectron spectroscopy (XPS) analysis at different etching times (Fig. S2); the results indicated that the chemical composition on the surface did not change during the procedure.

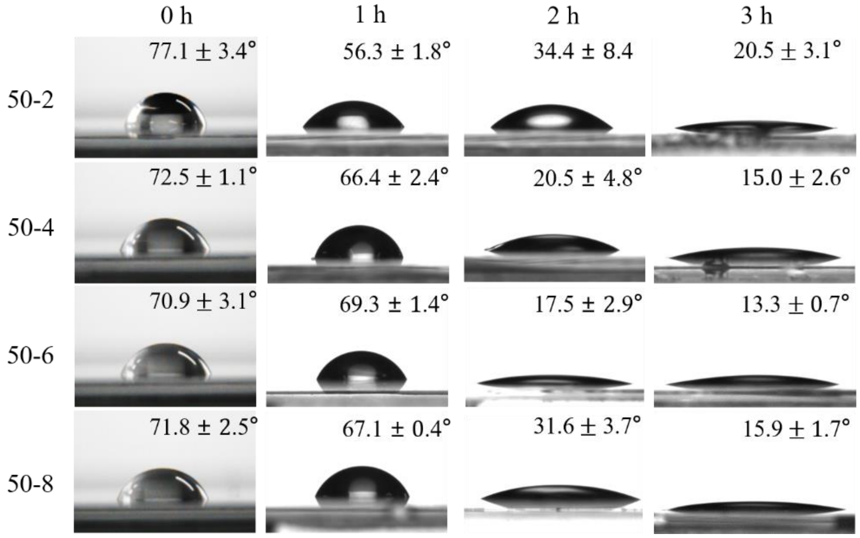

Fig. 3 Apparent water contact angle on BAFG surface with different microchannel widths and etching times. The droplet volume was 4 μL. The substrates were tested 3 times and the results were averaged to account for errors

3.3 Optical properties of the biomimetic structure

The transmittances of the glass substrates etched for 12 h are shown in Fig. 4. To clearly show the differences in transmittance with different circumcircle diameters and microchannel widths, the area fraction, *f*, of the microchannel was calculated using the following equation:

$$f = \mathrm{A_c}/\mathrm{A}, \tag{2}$$

where $\mathrm{A_c}$ denotes the projected area of the microchannel and A denotes the projected area of the glass substrate. The side length, *l*, of the micro-hexagon per unit area was also calculated using the following equation:

$$l = (A_{unit}/A_{hex}) \times S_{hex}, \tag{3}$$

where A_{unit} represents the projected area of the etched substrate with a square shape of side 10 mm, A_{hex} represents the area of the micro-hexagon calculated by using equation 4, and S_{hex} represents the perimeter of the micro-hexagon calculated by using equation 5.

$$A_{hex} = (3/4)d^2\sin 60°, \tag{4}$$

$$S_{hex} = 3d, \tag{5}$$

where d denotes the diameter of the outer circle of the micro-hexagon. Subsequently, l was nondimensionalized using the following equation:

$$L_i = l_i/(l_{200-8}), \tag{6}$$

where *i* represents the number of substrates (such as 200-8). This step compressed the data within a narrow range. Before testing the transparency of the BAFG substrate, the relationship between the transparency and etching time on a bare glass substrate was determined. It was found that as the etching time increased, the transparency initially increased and then decreased. When the etching time reached 12 h, the average transparency decreased to 78.2%, as shown in Fig. S4. Fig. 4a shows the transmittance of a glass substrate with different micro-hexagonal outer circle diameters and a constant microchannel width of 2 μm. These results showed that with an increase in the micro-hexagon outer circle diameter, both the area fraction of the microchannel, *f*, and the nondimensionalized length of the side of the micro-hexagon (per unit area), *L*, decreased; this resulted in an increase in transparency. To further investigate the influence of *L* on transparency, the etched substrate with the same *f* was tested, as shown in Fig. 4b. The results confirmed that transparency increased with decreasing *L*. The variation in transparency under the combined effect of *L* and *f* was also investigated (Fig. 4c). The results showed that increasing the microchannel width led to an initial decrease in transparency, followed by a subsequent increase; this is because the influence of the etched surface area, *f*, is larger than *L*.

The transparencies of all BAFG surfaces are shown in Fig. S5. All transmittances of the etched substrates were higher than 84% for the wavelength range of 390–780 nm. The average transmittance of No. 200-2 was greater than 99% of the baseline transmittance of bare glass from 418 to 631 nm. Therefore, the optimal performance was obtained when the circumcircle diameter and microchannel width were 200 and 2 μm, respectively. Using the data from the 200 μm circumcircle diameter, the transmittance decreased in the range of 390–700 nm and increased in the range of 700–780 nm as the channel width increased from 2 to 8 μm. With the decrease in wavelength from 780 to 390 nm, the etched substrates of all channel widths showed an increase in transmission to a maximum value, followed by a decrease in transmission to a minimum value, further followed by an increase in transmission. The transmittance, as well as the wavelengths of the maximum transmittance, changed with respect to the microchannel width. A similar trend was observed with the data from the other circumcircle diameters.

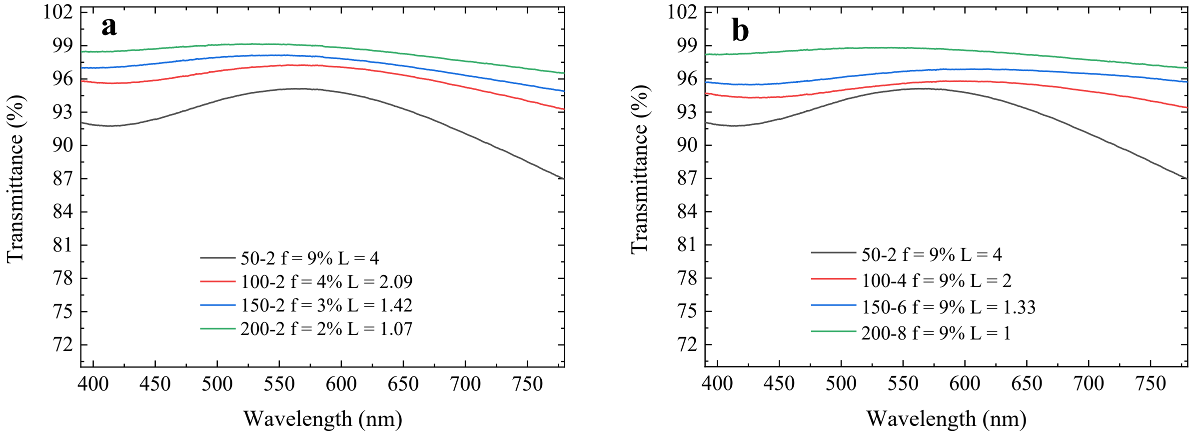

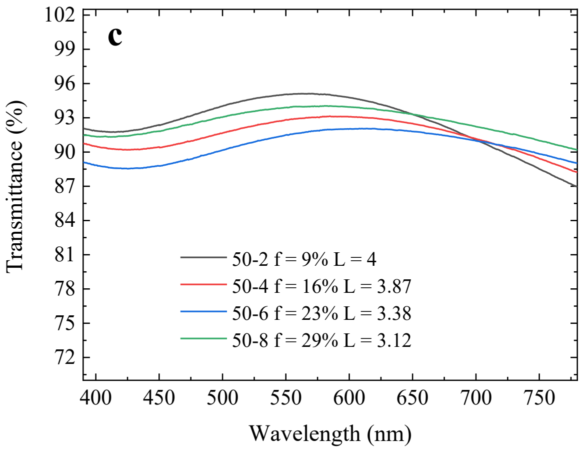

Fig. 4 Transmittances of substrates with different microstructures etched by KOH solution for 12 h with Cr mask only. **a** Relationship between transparency and circumcircle diameter. **b** Relationship between transparency and circumcircle diameter. **c** Relationship between transparency and microchannel width. 50-2 indicates that the diameter of the outer circle of the micro-hexagon is 50 μm and the microchannel width between the micro-hexagonal prisms is 2 μm. The area fraction of the microchannel (*f*) and the length of side of the micro-hexagon per unit area (*L*) are indicated in the legends

The transmittances of the glass substrates etched for 1 to 3 h after 12 h etching and removal of the Cr film are shown in Fig. 5. Under identical circumcircle diameters and microchannel widths, a decrease in the wavelength resulted in similar variations of the transmittances for the etched and non-etched glass substrates. The nonetched substrate corresponded to 0 h. The transmittances of the etched substrates increased with increasing microchannel width. When the microchannel width was 2 μm, the transmittance of the etched glass substrate was better than that of the nonetched substrate in the wavelength range of 650–780 nm. However, for the wavelength range of 390–700 nm, the transmittance of the same etched substrate was less than that of the non-etched surface. In addition, the transmittances of the etched glass substrates were generally better than those of the non-etched substrates when the microchannel widths were 4, 6 and 8 μm. Furthermore, when the microchannel widths were 4 and 8 μm, the transmittance decreased as the etching time increased. However, this was not the case when the width of the microchannel was 6 μm; this was because the second corrosion changed the intrinsic nanostructure and produced a hierarchical structure that improved the transmittance of the etched substrate. As the etching time increased, the thickness of the secondary structure increased, thereby decreasing the transmittance. By contrast, the new nanostructure induced by the second etching on the surface of the micro-hexagonal prisms reduced the transmittance, which affected the improvement in transmittance. However, the maximum variation in the transparency was 1.8%, which showed that the influence of the second etching was not obvious. When the wavelength was longer than the thickness of the nanostructure, the structure reduced the reflection and increased the transmittance. However, when the wavelength was shorter than the thickness of the nanostructure, the structure increased the reflection and reduced the transmittance [13].

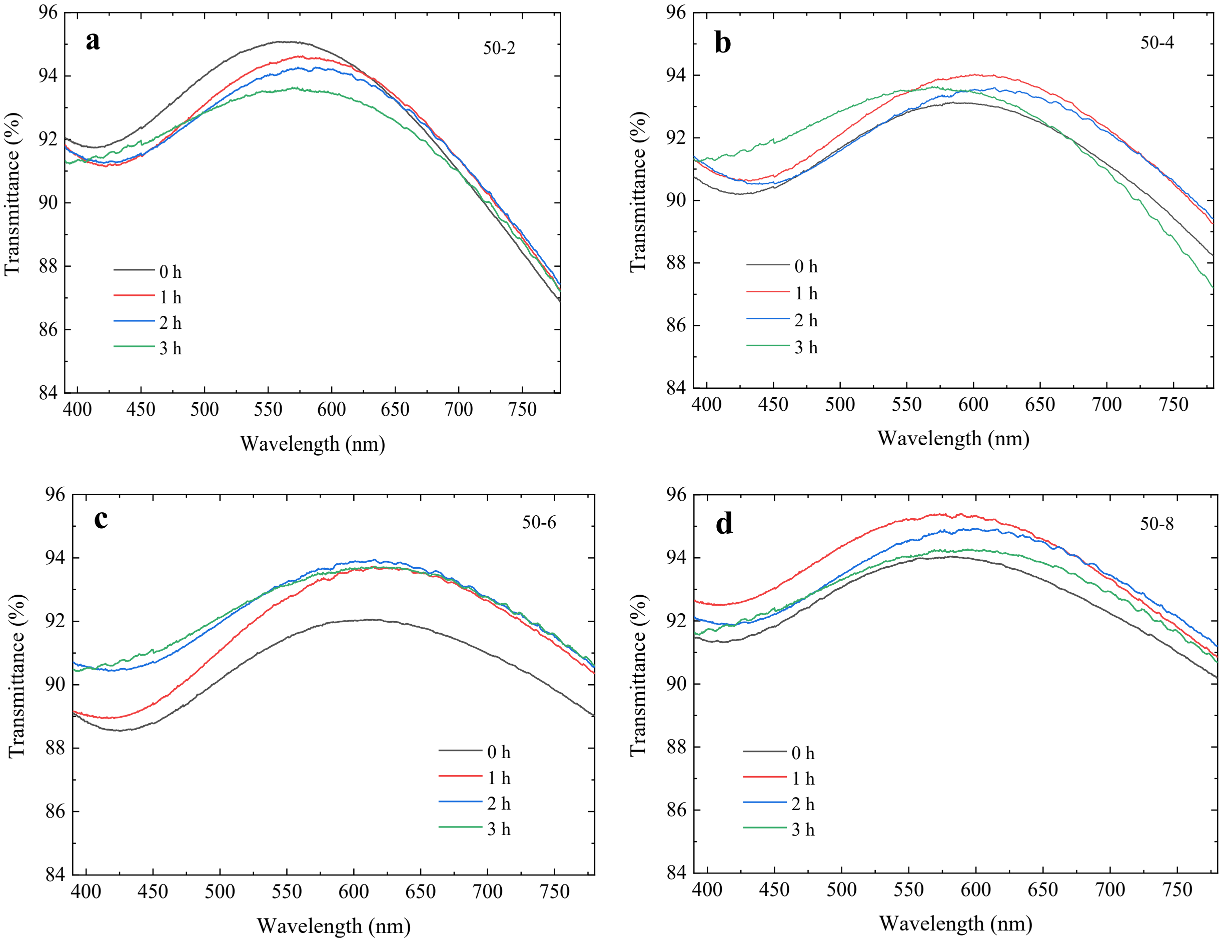

Fig. 5 Transparency of substrates etched by KOH solution for different durations (after etching by KOH solution for 12 h with Cr mask). The transparency of substrates with the diameter of the outer circle of micro-hexagon as 50 μm and microchannel widths of **a** 2 μm, **b** 4 μm, **c** 6 μm and **d** 8 μm were tested; these were immersed in KOH solution and heated to 95 ℃ for 1–3 h

3.4 Antifogging property of the biomimetic surface

The transparency differences of the BAFG surface and the slide glass are shown in Fig. 6a. The BAFG surfaces exhibited significantly high transmittances. When the temperature of a solid surface was less than or equal to the dew point temperature, the water vapor present in the air transformed into small and discrete liquid droplets on the solid surface [8]. The discrete droplets scattered the incident light in all directions, which significantly decreased the transparency of the optical materials. Etching of the biomimetic structure on the glass substrate created a hydrophilic surface that prompted the formation of a continuous thin water film, which resulted in high optical properties, as shown in Fig. 6b.

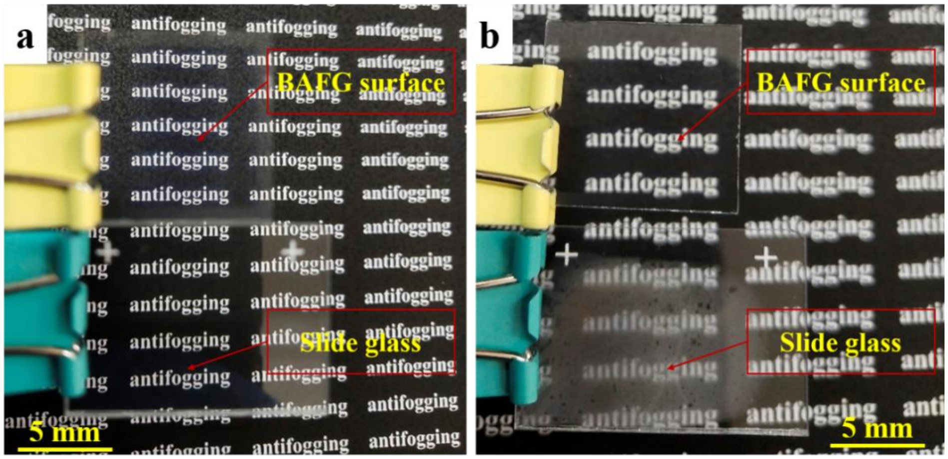

Fig. 6 a Comparison of the transparencies of BAFG surface and slide glass. **b** Comparison of the transparencies of bare glass and BAFG surface after steam exposure (from boiling water) for 30 s in an ambient environment with room temperature of 25 °C and relative humidity of 55%

To quantitatively investigate the antifogging property, the etched glass substrate was exposed to steam from boiling water for 30 s in an ambient environment with a relative humidity of 55% and temperature of 25 °C. The transparencies before and after exposure to steam were measured using a UV spectrophotometer in the wavelength range of 780 to 390 nm. In Fig. 7, the transmittance of bare glass after steam exposure is shown with a continuous black line; the transmittances of the etched substrate in the dry state and after steam exposure are shown with continuous and dashed lines of the same color for each microchannel width, respectively. Fig. 7a shows the relationship between the transmittance and wavelength of the glass substrate etched for 1 h. As shown by the dashed lines in Fig. 7a, the transparency slowly and continually approached the value of the dry substrate as the wavelength was decreased due to the fading of fog on the etched substrate. Moreover, the transparency of the etched substrate was higher than that of the glass slide after steam exposure. In particular, the etched substrate with a microchannel width of 6 μm exhibited the highest transparency. Fig. 7b shows the transparency as a function of wavelength after etching for 2 h. The transparencies of the etched substrates after steam exposure improved significantly and exceeded that of the dry substrates. The highest transparency was obtained when the microchannel width was 6 μm. However, the differences in transparency for the different microchannel widths were not significant. Fig. 7c shows that the transparencies of the etched substrates after steam exposure are better than that of the dry substrates. However, there was no significant improvement compared with that in Fig. 7b. Finally, the average transmittances for the steam exposed samples in the 390–780 nm wavelength range were calculated. The average transmittance of 68.7% for bare glass improved to 94.4% for the BAFG surface.

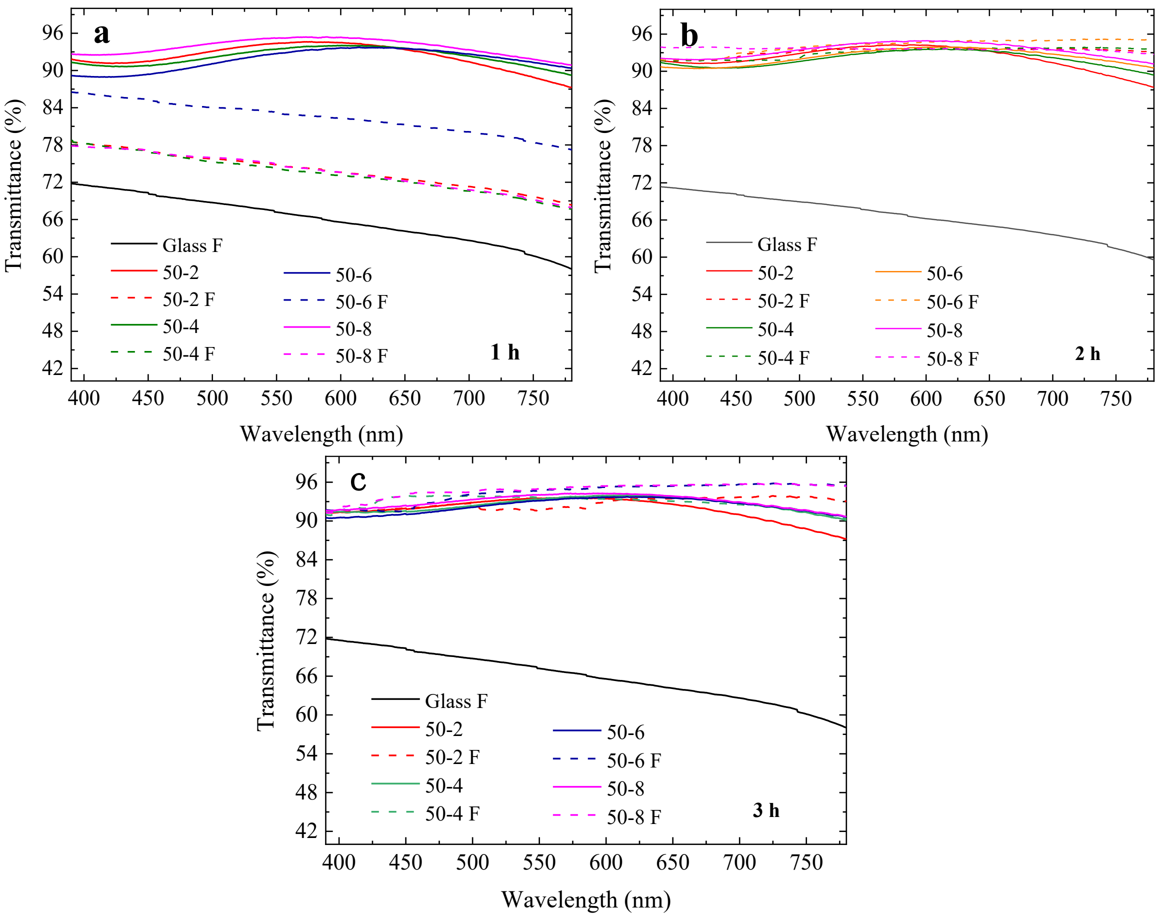

Fig. 7 Transparency of BAFG surface after exposure to steam for 30 s in an ambient environment with room temperature of 25 °C and relative humidity of 55% (etched by KOH solution for 12 h followed by removal of the Cr mask, etching 1−3 h). BAFG surface was immersed in KOH solution for **a** 1 h, **b** 2 h and **c** 3 h. The black continuous line represents the transparency of slide glass exposed to steam. The continuous lines marked with other colors represent the transparency of the dry BAFG surface. The dashed lines represent the transparency of the BAFG surfaces exposed to steam

To further explore the antifogging mechanism on the etched substrate, the condensation process was recorded using a digital microscope (Fig. 8). A semiconductor refrigeration chip was used to slowly reduce the BAFG surface temperature to the dew point temperature to clearly record the condensation process. The experiment was carried out at room temperature (25 °C) with a relative humidity of 55% and a temperature difference of 15 °C. The entire condensation process on the BAFG surface can be separated into three stages, as shown in Figs. 8a condensation, 8b condensation and collapse and 8c collapse. During the condensation stage, when the temperature of the glass substrate was less than or equal to the dew point temperature, the moisture in the surrounding air began to condense on the defects of the etched substrates, particularly in the microchannels, as shown in Fig. 8f. As the condensation process progressed, the nuclei grew and combined with each other to form a large embryo. The reflective intensity of the microchannel in Fig. 8f was stronger than that in Fig. 8e. During the condensation and collapse stages, the condensation process continued, and the droplets began to combine with each other to form a water film in the channels and on the top surface of the micro-hexagonal prisms. This film spread to the other microchannels on the BAFG surface via capillary action to form a water film network due to the narrow and rough microchannel surface. The BAFG surface was divided into several tiny plates by the water network. The droplets on the top surface of the micro-hexagonal prisms gradually increased in size and merged. Finally, when the droplets were sufficiently large, they collapsed. At this time (Fig. 8g), the three-phase contact line of the droplets on the partial top surface of the micro-hexagonal prisms broke through the energy barrier from the edges of the structure and connected with the water film network. Hence, the droplets were easily absorbed in the microchannels due to the wettability gradient. Since the condensation rate varies at different locations on the surface under external disturbances, the condensation and collapse processes occured simultaneously at 167 s. Finally, during the collapse stage, almost all droplets on the top surface of the micro-hexagonal prisms broke through the energy barrier from the edges of the structure and were absorbed in the water film network to form a single stable water film on the BAFG surface due to the interconnected microchannels. However, in the condensation process on the slide glass (Figs. 8a–d, Supporting videos 1 and 2), the nuclei grew and combined with each other to form a large embryo instead of a thin water film on the slide glass.

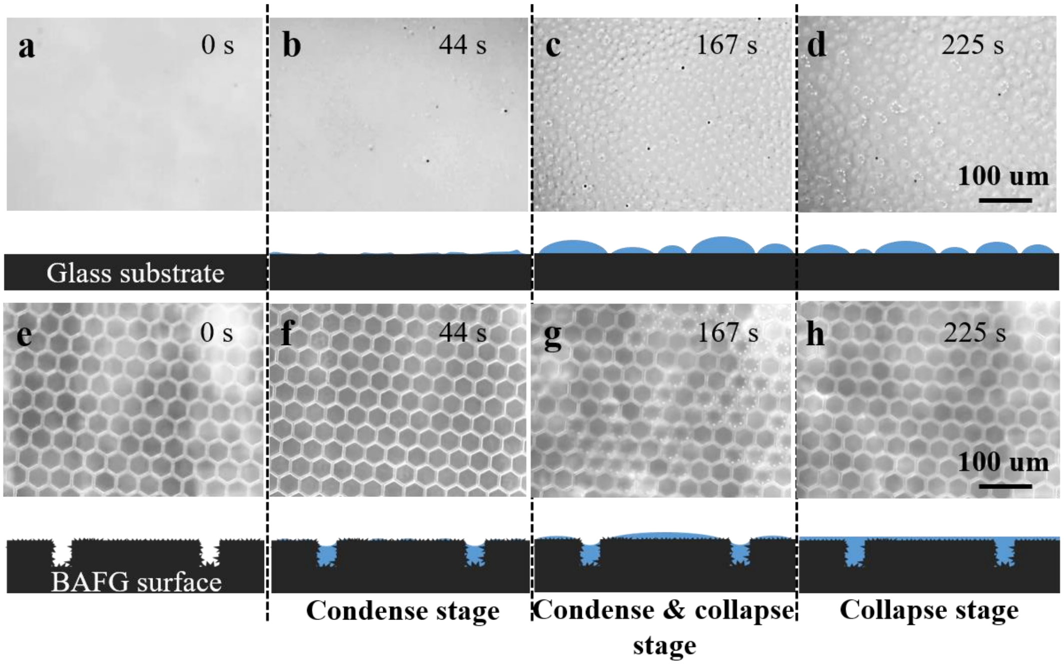

Fig. 8 Condensation process on the bare glass (a–d) and BAFG surfaces (e–h)

The formation of a water film network on the BAFG surface is the key step in maintaining a thin water film. This process was analyzed using the classical theory of thermodynamics. The condensation process on the BAFG surface can be regarded as heterogeneous nucleation on a fractal surface, which was influenced by the wetting properties and morphology of the substrate. According to the classical theory of nucleation, the change in free energy (ΔG) during condensation can be expressed as [47]:

$$\Delta \mathrm{G} = \Delta G_V V_l + \gamma_{gl} A_{gl} + (\gamma_{ls} - \gamma_{gs}) A_{ls}, \tag{7}$$

where γ_{gl}, γ_{ls} and γ_{gs} refer to the interfacial energies between the gas and liquid, liquid and solid, gas and solid, respectively, A_{gl} and A_{ls} refer to the corresponding interfacial areas, V_l

refers to the volume of the embryo, and ΔG_V refers to the change in the free energy per unit volume of the embryo from gas to liquid.

When nuclei gradually grow and combine with each other on the BAFG surface, the CA on the BAFG surface can be described by the Wenzel equation [11]:

$$\cos\theta_w = \phi\cos\theta = \phi(\gamma_{sg} - \gamma_{sl})/\gamma_{lg}, \tag{8}$$

where ϕ denotes the roughness parameter defined as the ratio of the practical surface area to the projected area, θ_w denotes the apparent CA, θ denotes the intrinsic CA.

As the embryo gradually grows, it can be considered as a spherical cap. Therefore, the volume, interfacial area and superficial area of the embryo were calculated using the spherical cap model, as shown in Fig. 9a.

$$\begin{cases} V_l = (\pi R^3/3)(2 - 3\cos\theta_w + cos^3\theta_w) \\ A_{gl} = 2\pi R^2(1 - cos\theta_w) \\ A_{ls} = \pi R^2\phi(1 - cos^2\theta_w) \end{cases} . \tag{9}$$

Referring to Eqs. (8) and (9), the energy change of nucleation on the fractal surface can be expressed as follows [47]:

$$\Delta \mathrm{G} = \left[(4\pi R^3/3)\cdot\Delta G_V + 4\pi R^2\cdot\gamma_{gl}\right]\cdot[(2 - 3\cos\theta_w + \cos^3\theta_w)/4]. \tag{10}$$

To calculate the critical radius of the embryo, Eq. (10) yields $d\Delta\mathrm{G}/dR = 0$ and the critical radius (R) can be calculated as:

$$\mathrm{R} = -2\gamma_{gl}/\Delta G_V. \tag{11}$$

Eq. (11) suggests that the roughness parameter has no effect on the critical radius of the embryo. Referring to Eqs. (10) and (11), the work of heterogeneous nucleation on a fractal surface can be calculated as:

$$\Delta G^* = \left(16\pi\gamma_{gl}^3/3\Delta\mathrm{G}_V^2\right)\times(2 - 3\cos\theta_w + \cos^3\theta_w)/4. \tag{12}$$

Eq. (12) depends on both the contact angle and roughness parameter ($\cos\theta_w$), which consists of homogeneous nucleation work, $\Delta G_h^* = \frac{16\pi\gamma_{ls}^3}{3\Delta\mathrm{G}_V^2}$, and a coefficient of $(2 - 3\cos\theta_w + \cos^3\theta_w)/4$. Hence, to investigate the influence of the roughness parameter on the heterogeneous nucleation, Eq. (12) can be nondimensionalized with homogeneous nucleation work and expressed as [48]:

$$\Delta G^*/\Delta G_h^* = (2 - 3\phi\cos\theta + \phi^3 cos^3\theta)/4. \tag{13}$$

Fig. 9b illustrates the relationship between the work of heterogeneous nucleation on the fractal surface and roughness parameter, ϕ, predicted by Eq. (13). When the intrinsic CA is less than 90°, the heterogeneous nucleation work decreases with increasing roughness parameter. Consequently, nucleation is likely to occur on rough hydrophilic surfaces. This theoretical result was consistent with the trend observed in the experimental data. In summary, the water film network divided the surface into several tiny plates and connected them; this allowed the embryo to cover the surface in a short period of time. Consequently, the embryo was absorbed by the water film network to form a stable water film on the entire BAFG surface. Such a mechanism adequately resolves the difficulty associated with the incident light scattering induced by discrete droplets formed during the condensation process.

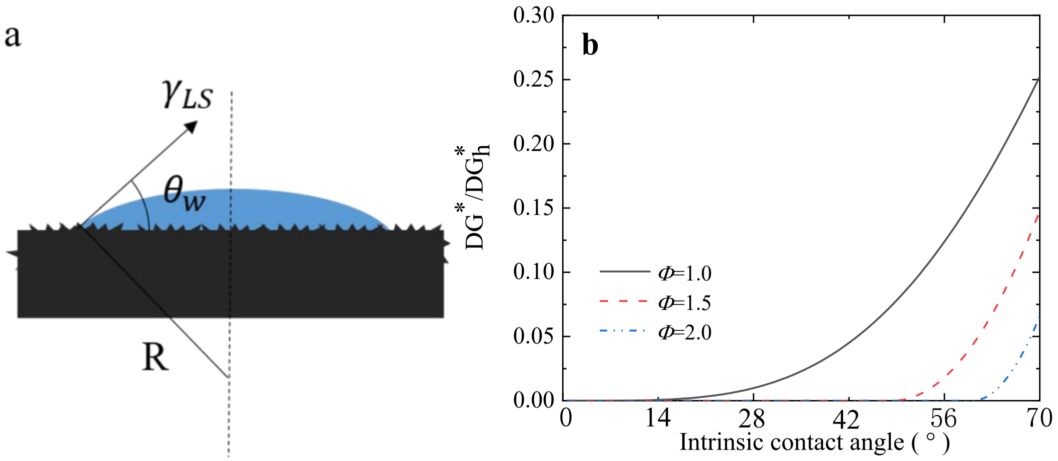

Fig. 9 a Schematic of the apparent CA and radius of an embryo on the fractal surface, where R denotes the radius of the embryo, θ_w denotes the apparent contact angle of the embryo, and γ_{ls} denotes the liquid-solid interfacial energy. **b** Influence of the roughness ratio on the heterogeneous nucleation work.

4. CONCLUSIONS

In this study, a BAFG surface was designed and manufactured through common UV lithography, ion beam etching, neutral loop discharge, and chemical etching. The prepared surface exhibited hydrophilic surface chemistry and an arrayed micro-hexagonal prism structure. The wettability, optical characteristics and antifogging properties of the BAFG surface were characterized experimentally. The BAFG surface exhibited excellent antifogging and optical properties. Remarkably, the transmittance of the BAFG surface reached 99% of the baseline transmittance of bare glass. In addition, the optical performances of the BAFG surfaces after steam exposure were quantitatively tested. Notably, the average transmittance of 68.7% for the bare glass improved to 94.4% for the BAFG surface after steam exposure. Furthermore, the mechanism of condensation was investigated by defining three consecutive stages and was analyzed using thermodynamics theory. This addressed the issue of incident light scattering induced by discrete droplets in the condensation process, and therefore significantly improved the optical transparency. Transmittances of the steam exposed BAFG surfaces were greater than those of the dry BAFG surfaces. Although details, such as the optimal structural parameters for anti-fog performance and durability of the substrate, have not been investigated here, this work provides a highly promising method to address the fogging problem and has potential applications in the aeronautical, automobile, and solar-energy sectors; this research was inspired by the excellent diffusivity of water from the tree frog toe pads and achieved a balance between surface wettability and optical properties.

ASSOCIATED CONTENT

Supporting Information. Additional experimental details, materials and methods, including photographs of the experimental setup.

ACKNOWLEDGMENTS

The authors would like to acknowledge the financial support from the National Nature Science Foundation of China (Grant Nos. 51879218 and 52071272), the Basic Research Program of Natural Science in Shaanxi Province (No. 2020JC18), Basic Frontier Projects (No. JCKY08×18) and Fundamental Research Funds for the Central Universities (No. 3102020HHZY030014).

REFERENCES

(1) M. Gallaway, J. Aimino, M. Scheiman, The Effect of Protective Sports Eyewear on Peripheral Visual Field and a Peripheral Visual Performance Task. J. Am. Optom. Assoc. 57 (4), 304-10 (1986)
(2) T. H. Margrain, C. Owen, The Misting Characteristics of Spectacle Lenses. Ophthal. Physl. Opt. 16 (2), 108-114 (1996)
(3) S. J. Dain, A. K. Hoskin, C. Winder et al., Assessment of Fogging Resistance of Anti-Fog Personal Eye Protection. Ophthal. Physl. Opt. 19 (4), 357-361 (1999)
(4) J. M. Crebolder, R. B. Sloan, Determining the Effects of Eyewear Fogging on Visual Task Performance. Appl. Ergon. 35 (4), 371-381 (2004)
(5) G. Croce, P. D'Agaro, F. Della Mora, Numerical Simulation of Glass Fogging and Defogging. Int. J. Comput. Fluid D. 19 (6), 437-445 (2005)
(6) K. M. Al-Khalil, T. G. Keith, K. J. De Witt, Modelling of Surface Water Behaviour on Ice Protected Aircraft Components. Int. J. Numer. Method H. 2 (1), 555-571 (1992)
(7) G. D. Herbage, Anti-Fog and Frost Coatings. Aircr. Eng. Aerosp. Tec. 44 (9), 49-& (1972)
(8) N. Agam, P. R. Berliner, Dew Formation and Water Vapor Adsorption in Semi-Arid Environments - A Review. J. Arid. Environ. 65 (4), 572-590 (2006)
(9) M. A. Fayazbakhsh, M. Bahrami, Analytical Modeling of Mist Condensation by Natural Convection over Inclined Flat Surfaces. In Book of Abstracts, ASME Summer Heat Transfer Conference (SHTC), Univ. Minnesota, Minneapolis, MN. 2014
(10) J. Xiong, S. N. Das, J. P. Kar, et al., A Multifunctional Nanoporous Layer Created on Glass through a Simple Alkali Corrosion Process. J. Mater. Chem. 20 (45), 10246-10252 (2010)
(11) R. N. Wenzel, Resistance of Solid Surfaces to Wetting by Water. Ind. Eng. Chem. 28, 988-994 (1936)
(12) R. N. Wenzel, Surface Roughness and Contact Angle. J. Phys. Colloid Chem. 53 (9), 1466-14679 (1949)
(13) X. Du, J. He, Structurally Colored Surfaces with Antireflective, Self-Cleaning, and Antifogging Properties. J. Colloid Interface Sci. 381, 189-197 (2012)
(14) T. Fujima, E. Futakuchi, T. Tomita, et al., Hierarchical Nanoporous Glass with Antireflectivity and Superhydrophilicity by One-Pot Etching. Langmuir. 30 (48), 14494-14497 (2014)
(15) Y. M. Song, G. C. Park, E. K. Kang, et al., Antireflective Grassy Surface on Glass Substrates with Self-Masked Dry Etching. Nanoscale Res. Lett. 8: 505 (2013)
(16) M. Domke, G. Sonderegger, E. Kostal, et al., Transparent Laser-Structured Glasses with Superhydrophilic Properties for Anti-Fogging Applications. Appl. Phys. A 125 (10) (2019)
(17) E. Kostal, S. Stroj, S. Kasemann, et al., Fabrication of Biomimetic Fog-Collecting Superhydrophilic-Superhydrophobic Surface Micropatterns Using Femtosecond Lasers. Langmuir. 34 (9), 2933-2941 (2018)
(18) H. Liu, L. Feng, J. Zhai, et al., Reversible Wettability of A Chemical Vapor Deposition Prepared Zno Film Between Superhydrophobicity and Superhydrophilicity. Langmuir 20 (14), 5659-5661 (2004)

(19) A. Borras, A. Barranco, A. R. Gonzalez-Elipe, Reversible Superhydrophobic to Superhydrophilic Conversion of Ag@Tio2 Composite Nanofiber Surfaces. Langmuir 24 (15), 8021-8026 (2008)
(20) D. Zheng, Y. Qiang, S. Xu, et al., Hierarchical MnO2 nanosheets synthesized via electrodeposition-hydrothermal method for supercapacitor electrodes. Appl. Phys. A 123 (2) (2017)
(21) J. V. Patil, S. S. Mali, J. S. Shaikh, et al., Hydrothermally grown 3D hierarchical TiO2 based on electrochemically anodized 1D TiO2 nanostructure for supercapacitor. Appl. Phys. A 124 (9) (2018)
(22) F. Yang, Z. Guo, B. Zhang, et al., A Co3O4/CuO composite nanowire array as low-cost and efficient bifunctional electrocatalyst for water splitting. Appl. Phys. A 127 (5) (2021)
(23) N. Lingappan, S. Lim, G.-H. Lee, et al., Recent advances on fiber-reinforced multifunctional composites for structural supercapacitors. Funct. Compos. Struct. 4 (1) (2022)
(24) J. W. Maina, J. M. Pringle, J. M. Razal, et al., Hierarchical hollow metal nanostructure arrays for selective CO2 conversion. Materials Advances 3 (5), 2456-2463 (2022)
(25) W. Shang, W. Yu, X. Xiao, et al., Self-Activated Formation of Hierarchical Co3O4 Nanoflakes with High Valence-State Conversion Capability for Ultrahigh-Capacity Zn-Co Batteries. Small 18 (12) (2022)
(26) Z. Sun, T. Shi, Y. Wang, et al., Hierarchical microencapsulation of phase change material with carbon-nanotubes/polydopamine/silica shell for synergistic enhancement of solar photothermal conversion and storage. Sol. Energy Mater. Sol. Cells. 236 (2022)
(27) S. Xiao, X. Hu, X. Jiang, et al., Enhanced thermal performance of phase change materials supported by hierarchical porous carbon modified with polydopamine/nano-Ag for thermal energy storage. J Energy Storage. 49 (2022)
(28) Z. Xie, H. Wang, M. Li, et al., Photothermal trap with multi-scale micro-nano hierarchical structure enhances light absorption and promote photothermal anti-icing/deicing. Chem. Eng. J. 435 (2022)
(29) C. Yin, L. Weng, Z.-X. Fei, et al., Form-Stable phase change composites based on porous carbon derived from polyacrylonitrile hydrogel. Chem. Eng. J. 431 (2022)
(30) L. Lei, L. Miao, H. Zheng, et al., Band gap extending of locally resonant phononic crystal with outward hierarchical structure. Appl. Phys. A-Mater. Sci. Process. 128 (6) (2022)
(31) Y. N. Rajeev, C. M. Magdalane, G. Ramalingam, et al., Photocatalytic activity of hierarchical CTAB-assisted TiO2 nanoparticles for polluted water treatment using solar light illumination. Appl. Phys. A 128 (4) (2022)
(32) W. Qiao, B. Jin, W. Xie, et al. Hierarchical CoNi-LDH nanosheet array with hydrogen vacancy for high-performance aqueous battery cathode. Journal of Energy Chemistry 69, 9-15. (2022)
(33) X. Ye, D. Cai, Y. Guo, et al., A Facile Method for Producing Superhydrophilic Glasses Via Charge Injection. Aip. Adv. 8 (12) (2018)
(34) C. Neinhuis, W. Barthlott, Characterization and Distribution of Water-Repellent, Self-Cleaning Plant Surfaces. Ann. Bot. 79 (6), 667-677 (1997)
(35) L. Feng, S. H. Li, Y. S. Li, et al., Super-Hydrophobic Surfaces: From Natural to Artificial. Adv. Mater. 14 (24), 1857-1860 (2002)
(36) X. F. Gao, L. Jiang, Water-Repellent Legs of Water Striders. Nature. 432 (7013), 36-36 (2004)
(37) X. Gao, X. Yan, X. Yao, et al., The Dry-Style Antifogging Properties of Mosquito Compound Eyes and Artificial Analogues Prepared by Soft Lithography. Adv. Mater. 19 (17), 2213-+ (2007)

(38) Z. Sun, T. Liao, K. Liu, et al., Fly-Eye Inspired Superhydrophobic Anti-Fogging Inorganic Nanostructures. Small. 10 (15), 3001-3006 (2014)

(39) C. Liu, J. Ju, Y. Zheng, et al., Asymmetric Ratchet Effect for Directional Transport of Fog Drops on Static and Dynamic Butterfly Wings. Acs Nano. 8 (2), 1321-1329 (2014)

(40) S. Feng, P. Zhu, H. Zheng, et al., Three-dimensional capillary ratchet-induced liquid directional steering. Science, 373 (6561), 1344-+ (2021)

(41) N. A. Dudukovic, E. J. Fong, H. B. Gemeda, et al., Cellular fluidics. Nature, 595 (7865), 58-+ (2021)

(42) G. Hanna, W. J. P. Barnes, Adhesion and Detachment of the Toe Pads of Tree Frogs. J. Exp. Biol. 155, 103-125 (1991)

(43) B. Murarash, Y. Itovich, M. Varenberg, Tuning Elastomer Friction by Hexagonal Surface Patterning. Soft Matter. 7 (12), 5553-5557 (2011)

(44) H. Chen, L. Zhang, D. Zhang, et al., Bioinspired Surface for Surgical Graspers Based on the Strong Wet Friction of Tree Frog Toe Pads. ACS Appl. Mater. Interfaces. 7 (25), 13987-13995 (2015)

(45) L. Xue, B. Sanz, A. Luo, et al., Hybrid Surface Patterns Mimicking the Design of the Adhesive Toe Pad of Tree Frog. Acs Nano. 11 (10), 9711-9719 (2017)

(46) L. Zhang, H. Chen, Y. Guo, et al., Micro-Nano Hierarchical Structure Enhanced Strong Wet Friction Surface Inspired by Tree Frogs. Adv. Sci. 7 (20) (2020)

(47) M. Wang, Y. Zhang, H. Zheng, et al., Investigation of the Heterogeneous Nucleation on Fractal Surfaces. J. Mater. Sci. Technol. 28 (12), 1169-1174 (2012)

(48) H. Zheng, M. Wang, X. Wang, et al., Analysis of heterogeneous nucleation on rough surfaces based on Wenzel model. Acta Phys. Sin. 60 (6), 066402-1-066402-6 (2011)